High-Frequency Mapping of Downward Shortwave Radiation From GOES-R Using Gradient Boosting

Sadegh Ranjbar, *Graduate Student Member, IEEE*, Danielle Losos, Sophie Hoffman, and Paul C. Stoy

***Abstract*—This study investigates high-frequency mapping of downward shortwave radiation (DSR) at the Earth's surface using the advanced baseline imager (ABI) instrument mounted on Geostationary Operational Environmental Satellite—R Series (GOES-R). The existing GOES-R DSR product (DSR_{ABI}) offers hourly temporal resolution and spatial resolution of 0.25°. To enhance these resolutions, we explore machine learning (ML) for DSR estimation at the native temporal resolution of GOES-R Level-2 cloud and moisture imagery product (5 min) and its native spatial resolution of 2 km at nadir. We compared four common ML regression models through the leave-one-out cross-validation algorithm for robust model assessment against ground measurements from AmeriFlux and SURFRAD networks. Results show that gradient boosting regression (GBR) achieves the best performance ($R^2 = 0.916$, RMSE $= 88.05$ W·m^{-2}) with more efficient computation compared to long short-term memory, which exhibited similar performance. DSR estimates from the GBR model through the ABI live imaging of vegetated ecosystems workflow (DSR_{ALIVE}) outperform DSR_{ABI} across various temporal resolutions and sky conditions. DSR_{ALIVE} agreement with ground measurements at SURFRAD networks exhibits high accuracy at high temporal resolutions (5-min intervals) with R^2 exceeding 0.85 and RMSE $=$ 122 W·m^{-2}. We conclude that GBR offers a promising approach for high-frequency DSR mapping from GOES-R, enabling improved applications for near-real-time monitoring of terrestrial carbon and water fluxes.**

***Index Terms*—Ameriflux, downward shortwave radiation (DSR), geostationary satellite, machine learning (ML), SURFRAD.**

I. Introduction

DOWNWARD shortwave radiation (DSR) at the Earth's surface has long been estimated using geostationary ("weather") satellites by combining measured top-of-atmosphere (TOA) reflectances with radiative transfer models [1], [2], [3], [4], [5]. The NOAA operational algorithm using observations from the advanced baseline imager (ABI) on the Geostationary Operational Environmental Satellite—R Series (GOES-R) provides hourly estimates of DSR [3] (hereafter DSR_{ABI}) despite scanning on 5-min intervals across the conterminous United States (CONUS) and 10-min intervals across the Western Hemisphere "full disk" [6], [7]. This hourly cadence complicates nascent efforts to apply geostationary remote sensing to estimate terrestrial carbon and water cycling in near-real time [8], [9], because additional approaches must be taken to infer hourly DSR at more frequent intervals, which introduce uncertainty [10]. The DSR_{ABI} product creates maps with 0.25° × 0.25° (0.25° = 27–28 km) spatial resolution over CONUS [11] when most ABI products are created at 2-km resolution at nadir, with many missing estimates that require uncertain gapfilling to obtain continuous data (see Fig. 1). Reduced solar radiation, cloud cover, aerosol concentration, atmospheric pollution, atmospheric moisture content, variations in surface albedo (reflectivity) and various other environmental factors can contribute to data loss in the DSR product. For instance, during winter, the DSR_{ABI} typically experiences approximately 2 h with 90% or more of valid pixels in an image, reflecting periods of relatively clearer atmospheric conditions conducive to accurate data collection.

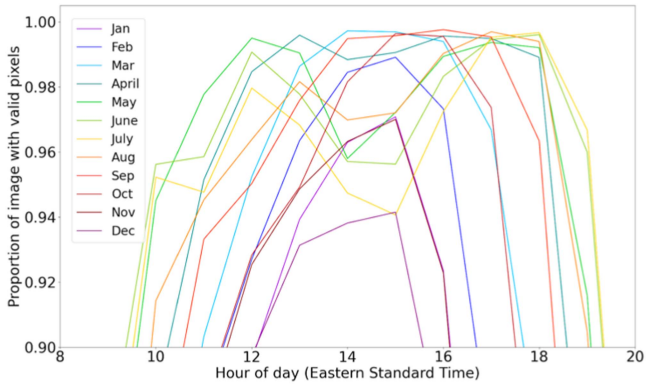

Fig. 1. Proportion of valid pixels in the DSR_{ABI} product from GOES-16 across the CONUS view in 2022, averaged over the course of the day for each month.

Recent work has applied machine learning (ML) to estimate DSR and/or photosynthetically active photon flux density from the observations of multiple geostationary satellites [5], [12], [13], [14], [15]. Artificial neural networks (ANNs), recurrent ANNs like long short-term memory (LSTM), random forest (RF), and deep learning approaches are often determined to have improved skill [12], [13], [16], [17], [18], [19], [20], due in part

Manuscript received 15 March 2024; revised 23 May 2024 and 20 June 2024; accepted 24 June 2024. Date of publication 27 June 2024; date of current version 12 July 2024. This work was supported in part by the University of Wisconsin–Madison Office of the Vice Chancellor for Research and Graduate Education with funding from the Wisconsin Alumni Research Foundation and in part by the National Science Foundation award 2106012. *(Corresponding author: Sadegh Ranjbar.)*

Sadegh Ranjbar, Danielle Losos, and Sophie Hoffman are with the Department of Biological Systems Engineering, University of Wisconsin–Madison, Madison, WI 53706 USA (e-mail: sranjbar@wisc.edu; losos@wisc.edu; shoffman22@wisc.edu).

Paul C. Stoy is with the Department of Biological Systems Engineering, University of Wisconsin–Madison, Madison, WI 53706 USA, and also with the Department of Atmospheric and Oceanic Sciences, University of Wisconsin–Madison, Madison, WI 53706 USA (e-mail: pestoy@wisc.edu).

Digital Object Identifier 10.1109/JSTARS.2024.3420148

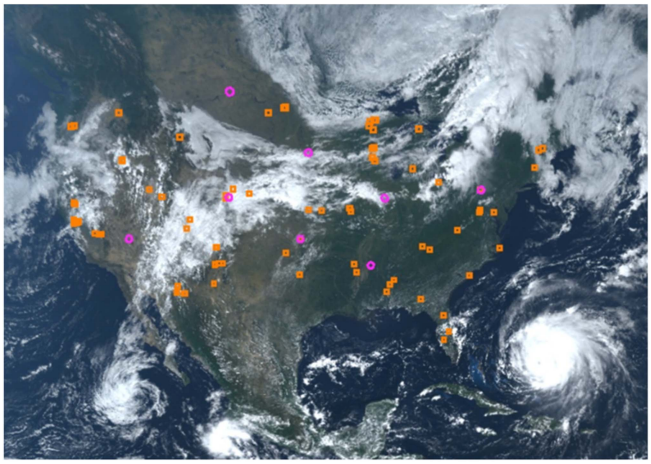

Fig. 2. Location of Ameriflux towers (orange squares) and SURFRAD sites (magenta circles) used in this study, mapped onto GOES-16 CONUS "true color" imagery from September 21, 2022.

to their ability to capture nonlinear relationships amongst multiple variables. Here, following the approach of [8] for carbon dioxide flux estimation using GOES-R, we demonstrate how gradient boosting regression (GBR) can give comparable skill in DSR estimation compared to more computationally expensive approaches like LSTM, multilayer perceptron neural networks (MLP), and RF to efficiently estimate DSR in near-real time from Level 2 cloud and moisture imagery (CMI) reflectance factors and brightness temperatures from the ABI across CONUS.

II. Data

We utilized ground measurements from the Ameriflux and NEON tower networks and SURFRAD networks, along with geostationary satellite observations obtained from the ABI sensor mounted on GOES-R series satellites. To create an efficient estimate of DSR using ABI data, we sampled time series of ABI Level 2 products at 99 sites across CONUS from pixels where Ameriflux eddy covariance towers are located that measure incident shortwave radiation (SW-IN) for the period 2020–2022 (see Fig. 2). Time series data collection followed the method proposed in [10], which applies a point-based terrain-correction to the ABI Fixed Grid projection to mitigate the effect of parallax displacement. The 2020–2022 period captures a range of atmospheric conditions across multiple climate zones for training and testing our model, hereafter $\mathrm{DSR}_{\mathrm{ALIVE}}$, following the ABI live imaging of vegetated ecosystems workflow [8]. The SW-IN measurements underwent consistent quality control (QC) checks through the standardized Ameriflux processing scheme [21]. These SW-IN data were combined with GOES-R ABI CMI observations, solar zenith angle (SZA), and solar azimuth angle (SAA) (SZA and SAA were calculated using NOAA solar position calculator[1]) to build a database of predictor variables (CMIs, SZA, and SAA) and target variables (SW-IN) to explore ML methods to estimate $\mathrm{DSR}_{\mathrm{ALIVE}}$. ABI CMI observations include 16 bands collected across the visible, near-infrared, and infrared ranges of the electromagnetic spectrum (see [6] and [7] for more specific information about the bands). The model performance was compared against independent SW-IN observations from the Ameriflux and NEON tower networks and SURFRAD [21], [22], [23]. The SURFRAD network measures DSR ($\mathrm{DSR}_{\mathrm{SURFRAD}}$) every minute, providing high-quality data at seven sites ideal for evaluating $\mathrm{DSR}_{\mathrm{ALIVE}}$ at various temporal intervals (refer to [22] for further information). The SURFRAD sites are located in seven different states across US (see Fig. 2), including Illinois (with site code of BND), Colorado (TBL), Nevada (DRA), Montana (FPK), Mississippi (GWN), Pennsylvania (PSU), South Dakota (SXF), and Oklahoma (SGP). We further compared $\mathrm{DSR}_{\mathrm{ALIVE}}$ with $\mathrm{DSR}_{\mathrm{ABI}}$, and $\mathrm{DSR}_{\mathrm{ABI}}$ to SW-IN, to understand differences that may arise between the different ABI-based data products. We analyzed data with respect to clear and cloudy skies using the ABI Clear Sky Mask product, and also explored the ability of the ABI aerosol optical depth (AOD) product to improve predictions [24], [25], noting that AOD estimates from the ABI also include frequent missing observations.

1.[Online]. Available at: https://gml.noaa.gov/grad/solcalc/calcdetails.html.

III. Methods

A. Regression Models: RF, GBR, LSTM, and MLP

We explored four common ML regression models to create $\mathrm{DSR}_{\mathrm{ALIVE}}$: RF, GBR, LSTM, and MLP [26], [27], [28].

RF and GBR, both ensemble models, blend decision trees via bootstrapping and feature bagging [29]. As applied in remote sensing [30], [31], [32], [33], they gauge feature importance but differ in focus. RF prioritizes simplicity and minimizing training set loss, while GBR emphasizes optimizing a loss function for error reduction. GBR iteratively constructs an additive model through a forward stage-wise approach, facilitating the optimization of diverse differentiable loss functions, while RF combines trees independently [30], [34]. Both require hyperparameter tuning, influencing model size and depth. In both models, shared hyperparameters include "number of estimators," "maximum depth," and "minimum samples per leaf." These parameters collectively determine model complexity, regularization, and generalization ability [20], [32], [34]. The "number of estimators" controls the quantity of decision trees in the ensemble, while "maximum depth" limits tree complexity to mitigate overfitting. "Minimum samples per leaf" sets the threshold for node splitting, aiding in regularization [32], [33]. Finally, the learning rate parameter modulates the contribution of each tree to the ensemble, fostering a balanced tradeoff between convergence speed and model stability [31], [34].

LSTM networks have proven instrumental in handling sequential data, showcasing proficiency in time series forecasting [35]. Their efficacy in capturing long-term dependencies, facilitated by unique memory cell architecture [36], [37], addresses a key limitation of traditional recurrent neural networks (RNNs) and can handle nonlinear relationships within sequences [37]. Despite their advantages, the complexity of LSTM architecture demands higher computational resources compared to simpler RNNs [38], [39]. In addition, achieving optimal performance

often requires careful hyperparameter tuning, adding intricacy to the training process [35]. Researchers must weigh these computational costs and tuning challenges against the benefits when applying LSTMs, to tailor an approach aligned with dataset characteristics and research goals [36], [37], [38], [39]. Our LSTM architecture utilized two LSTM layers with an identical number of units. The first layer ("return_sequences = True") retained and returned the entire sequence of hidden states for each input sequence, crucial for capturing temporal dependencies. Conversely, the second layer ("return_sequences = False") only returned the output at the last time step, effectively summarizing the learned information. Following the LSTMs, two dense layers were added. The first dense layer, with 25 units, facilitated further feature extraction and representation learning. The final dense layer, with a single unit, produced the model's output.

MLP is an ANN for learning patterns through backpropagation [40], [41], [42]. With layers of interconnected neurons and nonlinear activation functions, MLP is versatile in approximating nonlinear relationships [40], [42], [43]. Hyperparameters contribute to model complexity, nonlinear mapping, convergence speed, and preventing overfitting [44].

MLPs and LSTM networks rely on hyperparameters to optimize their performance. For MLPs, activation functions, solver algorithms, hidden layer configurations (including size), and regularization terms significantly impact the network's architecture, learning dynamics, and overfitting tendencies [36], [42]. In LSTMs, the number of units (neurons) determines memory capacity and computational complexity, while activation functions modulate information flow within memory cells [36]. Optimizer choice steers training dynamics and convergence, and batch size regulates efficiency and memory usage during training iterations [45], [46]. A mean squared error loss function was used for both MLP and LSTM.

B. Model Development

We used Google Colab Pro with random access memory up to 32 GB and an A100 graphics processing unit (GPU) for model development. To optimize model performance, we employed a grid search algorithm, systematically testing hyperparameter combinations within each ML model to identify configurations that maximize correlation (in terms of R^2) and prediction speed [28], [47]. Table I outlines the hyperparameter search specifications and ranges for each ML model.

For validation and evaluation, we adopted a leave-one-out cross-validation (LOOCV) algorithm, reserving 20% of the data exclusively for testing, while the remaining data underwent a four-fold cross-validation process with a 75:25 training-validation split [47]. To enhance reliability and robustness, we reran the algorithm ten times and averaged the results using the Scikit-learn Python library [48] and used the coefficient of determination (R^2) and root mean squared error (RMSE) to evaluate and compare models. Following model comparison, we used feature importance results to identify key variables for modeling DSR in a SHapley Additive exPlanations (SHAP) analysis [49].

TABLE I
GRID SEARCH SPECIFICATIONS AND HYPERPARAMETER SETTING FOR ML MODELS

Model	Hyperparameter	Grid Setting
RF	Number of estimators	100, 300, 500, 800, 1000
	Maximum depth	5, 8, 10, 15, 20, 30
	min_samples_leaf	50, 100, 200, 500
GBR	Number of estimators	100, 300, 500, 800
	Maximum depth	3, 5, 8, 10
	min_samples_leaf	50, 100, 200, 500
	Learning rate	0.01,0.05,0.1
MLP	Activation	"logistic", "tanh", "relu"
	Solver	"adam", "sgd"
	Hidden layer	2, 3, 5
	Hidden layer size	50, 100, 200, 500
	Alpha	0.0001, 0.001, 0.01, 0.1
LSTM	Units (neurons)	32, 64, 128, 256, 512
	Activation	"logistic", "tanh", "relu"
	Optimizer	"adam", "sgd"
	Batch Size	32, 64, 128, 256

SHAP is a powerful tool rooted in game theory for unraveling the opaque nature of ML predictions [49]. It uncovers individual feature contributions by quantifying the direction and magnitude of their influence to identify synergistic or antagonistic relationships that steer model behavior [50]. SHAP is not a universal solution; computational costs may scale with data size, and its effectiveness can be influenced by model complexity [51]. Nevertheless, SHAP can clarify individual predictions, unveil feature interactions, and demystify the "black box" nature of ML models. SHAP values are a unified measure to explain the output of ML models by quantifying the contribution of each feature to the prediction. Higher SHAP values denote features with more significant impact and importance on the model's predictions.

IV. RESULTS

A. ML Performance

The GBR and LSTM models displayed better performance than the other models with R^2 of 0.92, an improvement over the relationship between DSR_{ABI} against SW-IN observations for 314 Ameriflux sites (R^2 of 0.83 reported in [10]). The prediction time for LSTM is 19.5 times that of GBR (see Table II), which decreases to 4.2 times that of GBR with the use of Google Colab Pro A100 GPU. Given our objective of generating hypertemporal DSR maps from ABI imagery captured every 5 min, prediction time is critical. In this context, GBR emerged as the optimal choice among the ML models due to its similar accuracy and reduced prediction time compared to LSTM.

B. GBR Model Efficiency

To enhance the efficiency of prediction time versus accuracy, we conducted training experiments on the GBR model, varying the number of samples per site (with 20 965 available samples per site), the model parameters maximum depth (m_depth), and the number of estimators (n_estimators). We explored training

TABLE II
MODELS PERFORMANCE VERSUS PREDICTION TIME FOR ML MODEL TRAINING USING GOOGLE COLAB PRO

Model	Prediction Time	Train R^2	Train RMSE	Test R^2	Test RMSE
RF	CPU: 2.7 E-05 (2.2) A100 GPU: 2.7 E-05 (2.2)	0.90	93.41	0.884	105.68
GBR	CPU: 1.2 E-05 (1) A100 GPU: 1.2 E-05 (1)	0.93	84.33	0.916	88.05
MLP	CPU: 3.41 E-05 (2.8) A100 GPU: 2.5 E-05 (2.1)	0.90	95.78	0.888	101.15
LSTM	CPU: 23.4 E-05 (19.5) A100 GPU: 5.1E-05 (4.2)	0.92	85.09	0.914	87.52

Prediction time unit is seconds per sample. The number in parentheses is the relative prediction time compared to GBR. Units for RMSE are W m^{-2}.

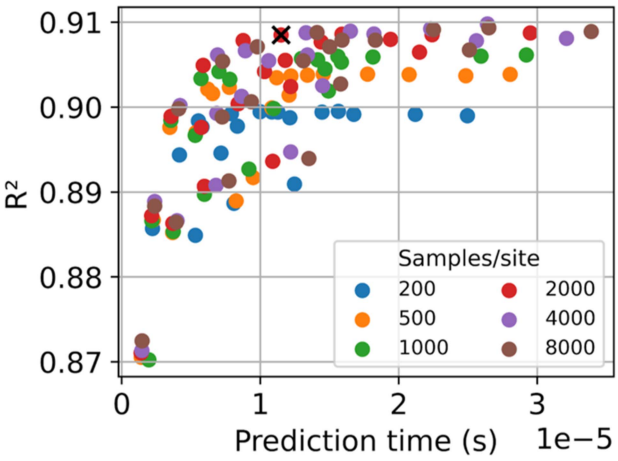

Fig. 3. R^2 score versus prediction time for GBR models (see Table II) with different m_depth, n_estimator, and training size. The black cross shows the selected GBR model that balances prediction time and accuracy.

with 200, 500, 1000, 2000, 4000, and 8000 samples per site, combinations of m_depth between 3, 5, 8, 10, and 12, and n_estimators of 100, 300, 500, 800, and 1000.

Models trained with 2000 samples per site exhibited better performance in terms of prediction time versus accuracy compared to those trained with 200, 500, or 1000 samples per site (see Fig. 3). Moreover, our analysis reveals that the model's performance stabilizes with 2000 samples per site, suggesting diminishing returns with larger sample sizes. Therefore, optimizing the sample size to balance accuracy and computational efficiency is paramount for our dataset generation objectives. Through iteration, we identified the most efficient GBR model, balancing prediction time (1.18E-5 s per sample) and correlation (R^2 of 0.91). This optimal model was trained with 2000 samples per site with m_depth = 8 and n_estimator = 300. The selection of this model is visually depicted by the black cross in Fig. 3. We used this model for $\mathrm{DSR_{ALIVE}}$.

A density scatter plot illustrating the relationship between SW-IN and $\mathrm{DSR_{ALIVE}}$ is shown in Fig. 4. The R^2 between half-hourly SW-IN and $\mathrm{DSR_{ALIVE}}$ is 0.92 with an RMSE of 86.12 W·m^{-2}.

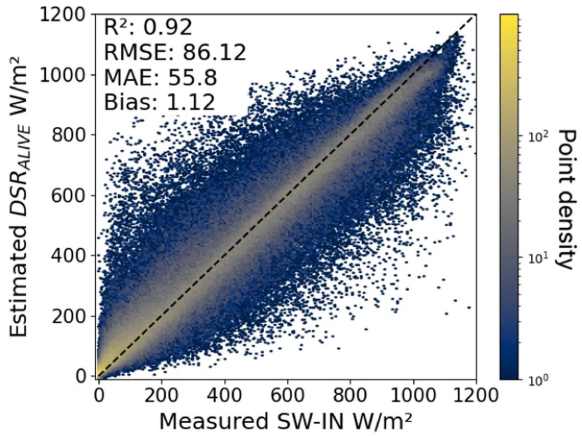

Fig. 4. Density scatter plot between half-hourly $\mathrm{DSR_{ALIVE}}$ and SW-IN measurements from eddy covariance towers.

TABLE III
$\mathrm{DSR_{ALIVE}}$ VERSUS AMERIFLUX TOWERS MEASUREMENTS AT TEMPORAL RESOLUTION AND SKY CONDITION

Temporal Resolution	Sky Condition	R^2	RMSE
Half hourly	clear	0.98	48.76
	cloudy	0.88	89.86
	all	0.92	86.12
Daily	all	0.99	10.30
Weekly	all	0.99	6.68

Table III presents the agreement of $\mathrm{DSR_{ALIVE}}$ versus SW-IN from the average of running LOOCV algorithm ten times. We computed R^2 and RMSE metrics by taking the mean DSR across different temporal resolutions (half-hourly, daily, and weekly) and sky conditions (clear and cloudy). Moreover, the daily analysis revealed a more robust performance of the GBR model when comparing estimated $\mathrm{DSR_{ALIVE}}$ to SW-IN, with R^2 values of 0.99, RMSE of 10.30 W·m^{-2}, MAE 8.19 and bias of -1.06 W·m^{-2}.

C. DSR_{ALIVE} Performance

The relationship between half hourly $\mathrm{DSR_{ALIVE}}$ and SW-IN has an R^2 value of 0.98 for clear skies and 0.88 for cloudy skies, with little bias as a function of local (standard) time (see Fig. 5). Bias for cloudy skies is larger, especially in the early morning.

Mean $\mathrm{DSR_{ALIVE}}$ largely matches SW-IN across the range of SZA from 11° to 88° (see Fig. 6) but slightly overestimates SW-IN at low SZA, especially in cloudy conditions [see Fig. 6(d)], noting that less training data are available at low SZA across CONUS [see Fig. 2].

D. Feature Analysis

We conducted SHAP analyses separately for clear and cloudy days and studied the top eight most impactful features on the

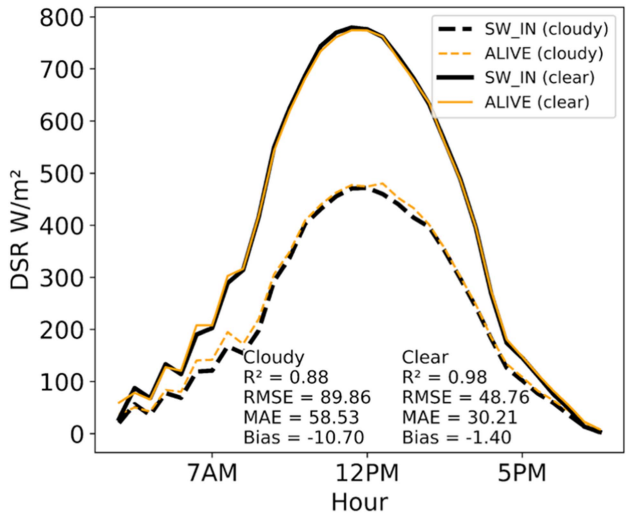

Fig. 5. Temporal performance of the GBR model at half-hourly intervals throughout the day under clear and cloudy conditions.

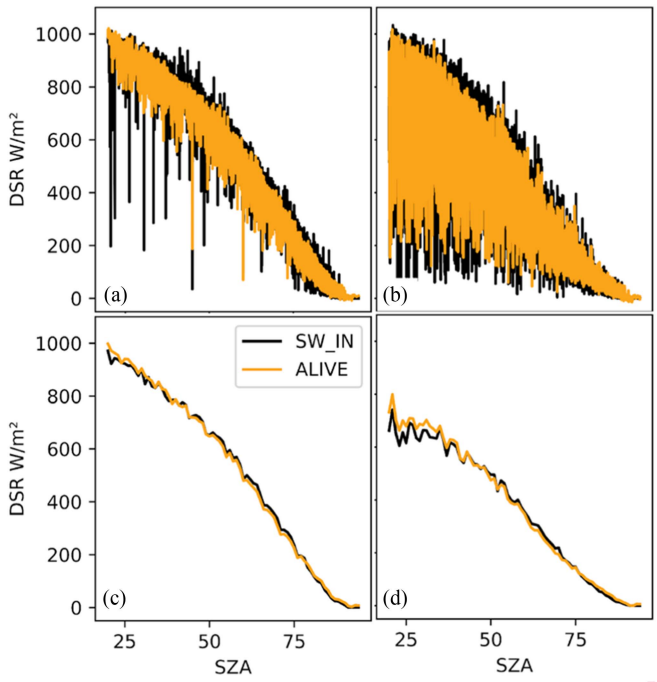

Fig. 6. Performance of the GBR model across varying SZAs on clear (a and c) and cloudy (b and d) days. SZA increments are 1° for panels c and d and 0.001° for panels a and b.

GBR model output for DSR predictions. SZA with the SHAP value of 0.79 is the most important, and CMI-C01 at wavelength of 0.47 μm (with SHAP value of 0.12) and SAA (with SHAP value of 0.04) consistently rank among the top three most important features for prediction (see Fig. 7). These features exhibit a positive correlation with the model prediction, where higher values result in higher DSR. Following these, CMI-C06 at wavelength of 2.2 μm, CMI-C15 at 12.3 μm, and CMI-C12 at 9.6 μm emerge as the next most important features for clear skies [see Fig. 7(a)], while for cloudy skies [see Fig. 6(b)], the order

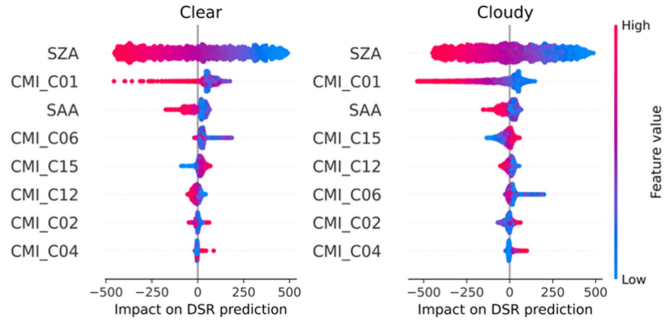

Fig. 7. SHAP analysis for relative feature importance for ML model inputs to predict DSR under clear (left) and cloudy (right) conditions.

of importance shifts to CMI-C15, CMI-C12, then CMI-C06. CMI-C15 displays a negative correlation impact on the model output, and CMI-C02 and CMI-C04 exhibit similar but smaller impacts as CMI-C15.

Our findings revealed a modest increase of 0.02 in the average R^2 when adding AOD to the GBR model. However, the standard deviation of R^2 values at a specific hour across all DOY increased by 0.05. Furthermore, 58% of our data was lost due to missing AOD pixel values. We expect there to be similar proportions of missing AOD data in the future because the ABI AOD algorithm has not changed. Using AOD as a predictor would, therefore, prevent DSR prediction at many timestamps, creating the same DSR data outages that we are aiming to prevent.

E. DSR_{ALIVE} Versus DSR_{ABI} Versus SW-IN: Assessment at Discrete Hours Across CONUS

Fig. 8 presents an analysis of the GBR model performance trained on data from 2021 and tested on 2022 data at a local standard time. By focusing on a specific hour on different DOY in 2022, from 99 sites spatially distributed across CONUS, we aimed to reduce the impact of time-based variations across the distributed sites. Each box plot in Fig. 8 represents the distribution of R^2 values obtained for a particular hour across all 365 DOYs in 2022, excluding periods without at least 80 sites in each computation.

$\mathrm{DSR_{ALIVE}}$ demonstrates higher R^2 values compared to $\mathrm{DSR_{ABI}}$ when compared with SW-IN throughout most hours, except for 6–8 P.M. local standard time (red box in Fig. 8), during which SZAs are characteristically low across the ABI CONUS scene (see Fig. 2). $\mathrm{DSR_{ALIVE}}$ and $\mathrm{DSR_{ABI}}$ deviate from SW-IN measurements after 5 P.M. [see Fig. 8(a) and (b)], and the mean R^2 between SW-IN and both $\mathrm{DSR_{ALIVE}}$ and $\mathrm{DSR_{ABI}}$ is less than 0.7 from 5 to 6 A.M. DSR averages less than 100 $\mathrm{W{\cdot}m^{-2}}$ during these times (see Fig. 5).

Fig. 9 presents the CONUS maps for estimated $\mathrm{DSR_{ALIVE}}$ and $\mathrm{DSR_{ABI}}$ at 6 P.M. UTC on September 21, 2022, providing a comparison extending beyond specific site locations. The analysis yielded R^2 of 0.83, RMSE of 132.15 $\mathrm{W{\cdot}m^{-2}}$, and bias ($\mathrm{DSR_{ABI}}$-$\mathrm{DSR_{ALIVE}}$) of 85.86 $\mathrm{W{\cdot}m^{-2}}$, notable differences between the two products across space and with respect to cloud characteristics revealed by storm systems. (Tropical Storm Ophelia can be seen on the right-hand side of the imagery.)

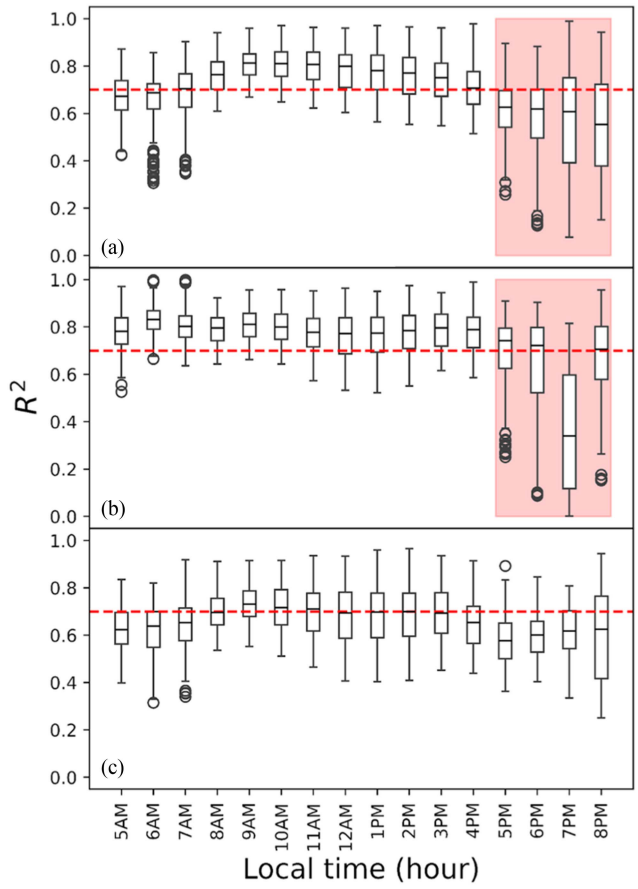

Fig. 8. R^2 values obtained for a specific hour (local standard time) across all DOY in 2022 using all the 99 sites distributed across CONUS. Plots present DSR_{ALIVE} predictions versus (a) tower SW-IN measurements and (b) the DSR_{ABI} product, and (c) the DSR_{ABI} product versus SW-IN measurements. The red dashed lines show an R^2 of 0.70. The red box signifies hours DSR_{ALIVE} showed lower performance than other hours.

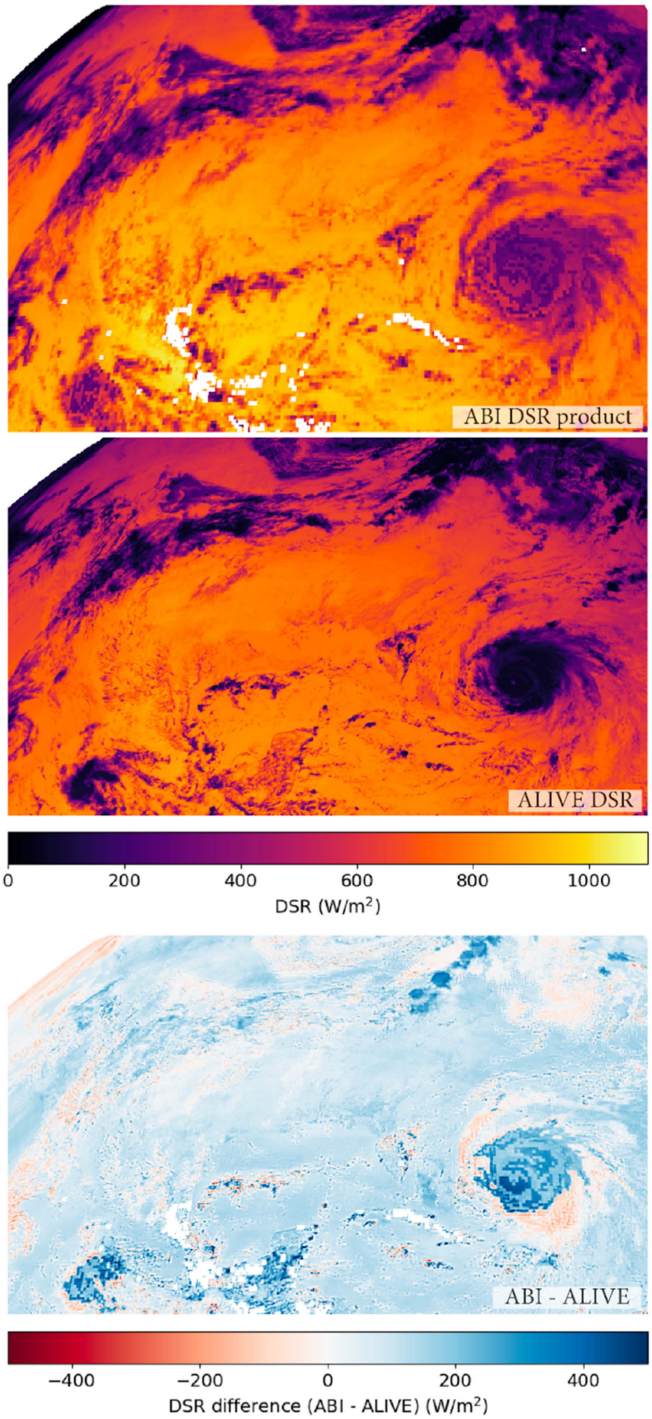

Fig. 9. DSR_{ABI}, estimated DSR_{ALIVE}, and their differences (ABI-ALIVE) maps at hour 6 P.M. UTC on September 21, 2022, with a CONUS view from the GOES satellite.

Fig. 10 compares the model performance at Ameriflux sites [see Fig. 10(a)] with the full images [see Fig. 10(b)] from Fig. 9 using kernel density estimates. SW-IN and DSR_{ALIVE} exhibit closer correspondence compared to their relationship with DSR_{ABI} [see Fig. 10(a)]. DSR_{ABI} typically shows higher estimates compared to the DSR_{ALIVE} [see Figs. 9 and 8(b)]. Fig. 10(a) and (b) depicts density plots related to September 21, 2022, at tower sites, where DSR_{ALIVE} and DSR_{ABI} maps are available (see Fig. 9). However, there is an observed bias of 85.86 $W{\cdot}m^{-2}$ between DSR_{ALIVE} and DSR_{ABI} maps which is evident in both the density plot [see Fig. 10(b)] and the difference between the two maps, DSR_{ABI} - DSR_{ALIVE} [see Fig. 9 (ABI-ALIVE)].

F. DSR_{ALIVE} Performance at 5-min Frequency Versus $DSR_{SURFRAD}$

We exclusively utilized $DSR_{SURFRAD}$ for testing DSR_{ALIVE}; none were used in training. We selected the first week of July 2022 for time series comparison (see Fig. 11) and assessed DSR_{ALIVE} performance across time intervals of 5, 15, and 30 min, as well as 1 and 2 h (see Table IV). Fig. 11 illustrates significant fluctuations in $DSR_{SURFRAD}$ at most sites, indicating the potential influence of aerosols or clouds [16], [52]. Analysis of AOD plots on the NOAA website, accessible at [53], further demonstrates substantial fluctuations in AOD values at these times and locations.

Fig. 11 indicates that the site DRA exhibits the highest agreement with an R^2 value of 0.98, followed closely by SXL, BND,

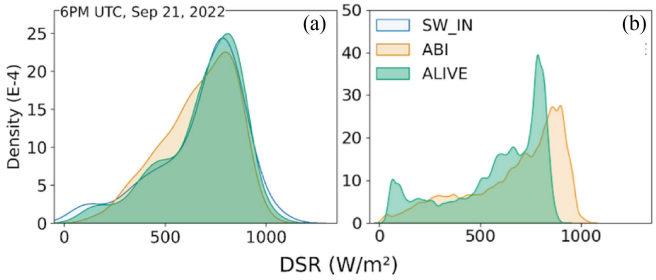

Fig. 10. Comparison of DSR distribution using kernel density estimate: SW-IN versus DSR_{ABI} versus DSR_{ALIVE} at 6 P.M. UTC on September 21, 2022, at (a) Ameriflux sites and (b) across CONUS from maps presented in Fig. 9.

TABLE IV
DSR_{ALIVE} VERSUS SURFRAD MEASUREMENTS

	5 min	15 min	30 min	1 h	2 h
R^2	0.85	0.86	0.88	0.90	0.91
RMSE	121.82	108.83	103.02	96.85	92.65
MAE	84.32	74.1	71.85	69.14	65.65
Bias	8.02	6.12	6.23	6.1	6.41

and TBL, each with R^2 values exceeding 0.85. In contrast, FPK and PSU display lower R^2 values of 0.77 and 0.79, respectively.

Table IV presents the accuracy of DSR_{ALIVE} versus $DSR_{SURFRAD}$ across temporal intervals ranging from 5 min to 2 h. As temporal resolution increases, there is a corresponding improvement in model performance, demonstrated by higher R^2 values and reduced error metrics such as RMSE, MAE, and Bias. However, one may consider R^2 values of 0.85 at a 5-min temporal resolution to be promising for hypertemporal analysis, effectively capturing short-term variations in DSR, noting that variability at shorter temporal scales, due to subpixel clouds and/or fast-moving clouds, will not be able to be resolved by the ABI.

V. DISCUSSION

A. ML Performance and Efficiency

Our study highlights the importance of selecting efficient ML models for predicting high-frequency DSR maps from ABI imagery. GBR emerged as the optimal choice, offering similar accuracy to LSTM but with substantially faster prediction time, crucial for real-time applications [54], [55]. Through optimization experiments, we identified a GBR model configuration that balances prediction time and accuracy, making it well-suited for generating "hypertemporal" DSR maps for our objective.

The findings from the GBR model efficiency experiment suggest that models trained with a larger volume of training data per site (2000 samples compared to 200, 500, or 1000) enhance the balance between prediction time and accuracy, thereby increasing overall model efficiency. Although it is well-known that a larger sample size improves ML performance [47], our study shows that it also increases efficiency in terms of prediction time. However, 2000 samples per site appear to be the saturation point for efficiency (see Fig. 3). Increasing the number of samples beyond this point increases training time with little improvement in fit. Furthermore, we observed that models with higher complexity (m_depth) and lower ensemble size (n_estimators) achieve optimization in both computational efficiency and predictive accuracy (see Fig. 3).

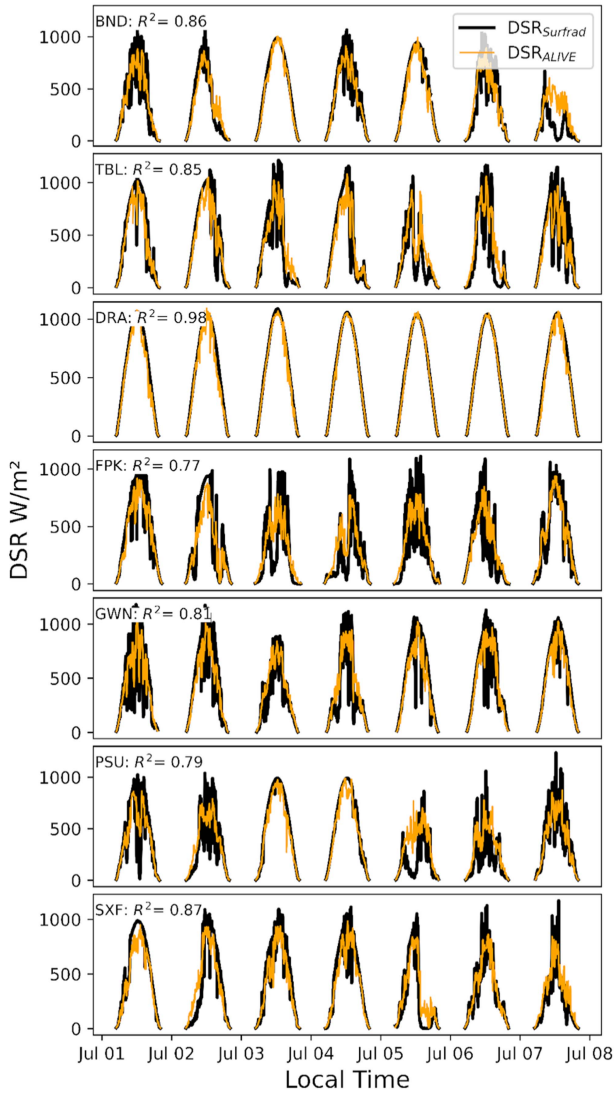

Fig. 11. Time series of DSR_{ALIVE} versus $DSR_{SURFRAD}$ at seven sites with a 5-min frequency during the first week of July 2022. Sites abbreviations and R^2 between DSR_{ALIVE} and $DSR_{SURFRAD}$ measurements are noted.

B. SHAP Analysis

SZA emerges as the most critical predictor for modeling DSR, as widely demonstrated in previous studies [15], [16], [17], [52]. Following SZA, CMI-C01, and SAA are significant predictors (see Fig. 7). These features demonstrate positive correlations with DSR, where higher values indicate higher DSR. CMI-C01, which measures blue visible reflectance at 0.47 μm; its importance is consistent with Rayleigh scattering [15], [56], [57], [58]. SAA improved time alignment of ABI observations with SW-IN measurements acquired at towers (see Fig. 5). This improvement addresses the timing issue previously described in detail by

Losos et al. [10]; in brief, the Ameriflux SW-IN observations represent an average between observations made at the top of the hour and half past the hour (or vice-versa) such that 15 and 45 min past the hour represents the average time over which observations are averaged. Time alignment was poorer before including SAA (results not shown).

Accurately estimating DSR presents a challenge influenced by factors beyond just cloud cover. Research in [24], [59], and [60] underscores the significant impact of cloud properties—like type, thickness, and composition—on solar radiation reaching the Earth's surface. In addition, AOD, as described in [5], [15], [24], [25], [60] in measuring atmospheric particle concentration, also affects solar radiation attenuation. Although Hao et al. [15], Ma et al. [16], and Hou et al. [61] showed the significance of using AOD in DSR modeling, incorporating AOD into the model results in only a modest increase in R^2 (0.02) for temporal patterns, but decreases R^2 between spatially distributed sites at specific hours, indicating prediction instability. Furthermore, the significant loss of data due to missing AOD values (approximately 58%) raises concerns about the reliability of the final DSR map at 5-min frequency. In addition to AOD, many studies [15], [16], [59], [62] show that cloud optical depth (COD), and cloud fraction (CF) also play crucial roles in DSR/PAR modeling. Here we assume that the ML model incorporates observations from the ABI TOA product (CMIs) for representing the impacts of AOD, COD, and CF in DSR modeling. Previous research indicates that CMI observations, particularly the blue band, contain valuable information regarding AOD levels. In 2022, Kang et al. [63] utilized GOCI geostationary satellite data to improve retrievals of AOD using a light GBR model. They achieved R^2 of 0.92 by showing CH01 (the GOCI blue band at 0.412 μm) as the most informative feature. Remote sensing, combined with ML, offers an effective tool for retrieving cloud microphysical parameters such as COD and CF [64], [65].

The comparison between $\mathrm{DSR_{ABI}}$ and $\mathrm{DSR_{ALIVE}}$ maps (see Fig. 9) reveals notable disparities, particularly in regions with high cloud cover, such as during hurricanes (Tropical Storm Ophelia is depicted on the southeast corner of Fig. 9). It is important to note that $\mathrm{DSR_{ABI}}$ products may not be a perfect reference for validation (with absolute error of up to 125 $\mathrm{W{\cdot}m^{-2}}$ [11]), especially in areas with frequent cloud cover or over oceans due to the lack of ground stations. Incorporating additional variables related to clouds, such as COD and/or CF, may enhance performance. However, relying on additional datasets would make $\mathrm{DSR_{ALIVE}}$ more vulnerable to data outages. Therefore, we have concluded that maintaining the simplicity of our algorithm is advisable, especially considering its effective performance compared to measurements of SW-IN measurements from towers.

C. Data Sources and Uncertainty: Ameriflux Versus SURFRAD

SURFRAD DSR measurements have lower uncertainty ($\pm$2% to $\pm$5%), compared to AmeriFlux's stated $\pm$10% uncertainty for net radiation observations [22]. However, AmeriFlux implements the AmeriFlux QC method to ensure data quality [21], [66], [67] and employs a multistep QC process to guarantee the integrity of eddy covariance and micrometeorological data [66], [68]. Following initial processing by tower teams, data undergo rigorous assessment encompassing individual variable inspection, evaluation of correlations between coupled variables (e.g., solar radiation and photosynthetically active radiation), analysis of temporal patterns, and in-depth examinations of interrelated variable variations [21], [68].

Interestingly, despite the difference in uncertainty, our research showed good agreement (R^2 of 0.85–0.91) between models trained on AmeriFlux data and DSR measurements from the SURFRAD network. This agreement held even at 5-min intervals, even though the models were trained on half-hourly data (see Table IV). This suggests that AmeriFlux SW-IN data, despite higher reported uncertainty, can be valuable for modeling purposes.

D. DSR_{ALIVE} Performance Against SW-IN, DSRABI, and $DSR_{SURFRAD}$

We observed that $\mathrm{DSR_{ALIVE}}$ generally outperformed $\mathrm{DSR_{ABI}}$ when compared with SW-IN measurements, except during specific evening hours characterized by high SZAs (see Fig. 8). In fact, both models performed more poorly compared to SW-IN measurements after 5 P.M., suggesting limitations in ABI to capture solar radiation dynamics during certain times of the day with high SZAs. DSR maps across CONUS in Fig. 9 revealed notable spatial differences between $\mathrm{DSR_{ALIVE}}$ and $\mathrm{DSR_{ABI}}$ products, particularly regarding their response to cloud characteristics. While $\mathrm{DSR_{ALIVE}}$ showed promising performance under clear sky conditions for data collected at the Ameriflux sites, differences persisted especially during periods of low solar radiation and in the presence of clouds.

Our findings demonstrate that $\mathrm{DSR_{ALIVE}}$ exhibits promising performance in estimating DSR at high temporal resolutions (5-min intervals) compared to ground-based measurements from the SURFRAD network (see Table IV). This is particularly significant because, to our knowledge, this is the first study to explore DSR mapping at such fine time scales. Traditionally, DSR retrievals have been limited to coarser temporal resolutions (half-hourly or hourly) due to constraints imposed by satellite data availability and/or processing techniques [5], [15], [16], [59], [69]. The ability of $\mathrm{DSR_{ALIVE}}$ to capture observed short-term variations holds significant value for various applications. For instance, monitoring rapid phenomena like heatwaves [70], [71], wildfires [72], [73], [74], water stresses and flash droughts [75], [76], and other fast-changing environmental events often necessitates high-frequency data. Similarly, studies investigating the carbon cycle or other processes sensitive to short-term fluctuations in solar radiation benefit from high-resolution DSR data [8], [77], [78], [79]. Our work paves the way for utilizing $\mathrm{DSR_{ALIVE}}$ as a tool to analyze these critical Earth system processes at unprecedented temporal detail.

It is important to note that while SURFRAD provides valuable ground-truth data, its network primarily focuses on mid-latitude regions (see Fig. 2). This poses a limitation for validating models like $\mathrm{DSR_{ALIVE}}$, which might struggle to simulate DSR

accurately at lower latitudes with lower SZAs (e.g., Fig. 6). These limitations in the SURFRAD network highlight the need for complementary validation strategies, potentially including future ground stations at lower latitude sites, to ensure the robustness of DSR_{ALIVE} and similar approaches across more geographical regions.

E. Comparing Against Recent Studies on DSR

At half-hourly resolution, our GBR models showed impressive performance metrics against Ameriflux sites (see Table III). Under clear sky conditions, our models achieve an R^2 of 0.98 with an RMSE of 48.76 $W{\cdot}m^{-2}$, surpassing the performance of DenseNET and CNNGRUnor architectures [17]. In cloudy sky conditions, although the R^2 slightly decreased to 0.88, the RMSE increased to only 89.86 $W{\cdot}m^{-2}$. Overall, our model's performance under all conditions at half-hourly resolution yields an R^2 of 0.92 and an RMSE of 86.12 $W{\cdot}m^{-2}$, indicating improved accuracy in comparison to recent studies [17], [19], [52], [69], [80]. For hourly DSR mapping, the GBR model demonstrates robust accuracy (see Fig. 4) compared to previous studies. In [52], researchers achieved an R^2 of 0.90 using a combination of GOES-16 and MODIS data and employing a look-up table at a 500-m spatial resolution. In addition, in another study, researchers achieved an R^2 of 0.82 using a combination of DSCOVR-EPIC data and employing an RF model for hourly DSR mapping at a 10 km spatial resolution [15].

Shifting to performance on daily time scales, our model also outperforms compared to [5] and [15], who achieved an R^2 of 0.88 and 0.93 compared to our daily R^2 of 0.99 (see Table III). Our GBR models exhibit exceptional accuracy with an R^2 of 0.99 and an RMSE of 10.30 $W{\cdot}m^{-2}$, outperforming the RF model from [19], which achieved an R^2 of 0.97 and an RMSE of 17.64 $W{\cdot}m^{-2}$. At a weekly resolution, our models maintain high accuracy, with an R^2 of 0.99 and an RMSE of 6.68 $W{\cdot}m^{-2}$. The robustness of our GBR models in terms of prediction time versus model performance for estimating DSR from GOES-R ABI data has significant implications for near-real-time carbon uptake mapping and solar energy applications.

When comparing DSR_{ALIVE} against $DSR_{SURFRAD}$, high agreement (R^2 of 0.85) is achieved even at 5-min frequency, although the GBR model was trained on half-hourly data from the AmeriFlux network. To the best of our knowledge, there is no other DSR product available at a 5-min frequency for comparison.

VI. Conclusion

We used public, quality-checked SW-IN ground measurements to train an ML model for predicting DSR at the native temporal and spatial scale of GOES-16 ABI CMI measurements. Our model outperformed the existing DSR_{ABI} algorithm under most solar conditions, with opportunities for improvement, especially at lower SZA and early morning/late evening periods. Additional surface SW-IN observations in subtropical and tropical regions for model training, and ongoing efforts to use ML to improve physically based atmospheric attenuation models, would likewise advance DSR product development to better realize the extensive benefits of geostationary satellite observations.

Acknowledgment

The authors are grateful to the AmeriFlux Management Project (AMP) and eddy covariance data providers, and the developers of the DSR_{ABI} product. The authors gratefully acknowledge Jeffry Ely for providing the NOAA Solar Position Calculator, which was used to compute the solar zenith angle (SZA and solar azimuth angle (SAA in this study (https://github.com/NASA-DEVELOP/dnppy/blob/master/dnppy/solar/README.md). The authors would also like to thank the editors and reviewers for their invaluable feedback and efforts in improving the quality of this article.

References

[1] G. R. Diak and C. Gautier, "Improvements to a simple physical model for estimating insolation from GOES data," *J. Clim. Appl. Meteorol.*, vol. 22, pp. 505–508, 1983.

[2] C. Gautier, G. Diak, and S. Masse, "A simple physical model to estimate incident solar radiation at the surface from GOES satellite data," *J. Appl. Meteorol. Climatol.*, vol. 19, no. 8, pp. 1005–1012, 1980.

[3] I. Laszlo, H. Liu, H.-Y. Kim, and R. T. Pinker, "Shortwave radiation from ABI on the GOES-R series," in *The GOES-R Series*. Amsterdam, The Netherlands: Elsevier, 2020, pp. 179–191.

[4] H.-Y. Kim, I. Laszlo, and H. Liu, "Shortwave radiation budget products from GOES-R Series ABI," in *Proc. IEEE Int. Geosci. Remote Sens. Symp.*, 2020, pp. 6698–6701.

[5] H. Zhang et al., "Retrieving high-resolution surface photosynthetically active radiation from the MODIS and GOES-16 ABI data," *Remote Sens. Environ.*, vol. 260, 2021, Art. no. 112436.

[6] T. J. Schmit, P. Griffith, M. M. Gunshor, J. M. Daniels, S. J. Goodman, and W. J. Lebair, "A closer look at the ABI on the GOES-R series," *Bull. Amer. Meteorol. Soc.*, vol. 98, no. 4, pp. 681–698, 2017.

[7] T. J. Schmit and M. M. Gunshor, "ABI imagery from the GOES-R series," in *The GOES-R Series*. Amsterdam, The Netherlands: Elsevier, 2020, pp. 23–34.

[8] S. Ranjbar, D. Losos, S. Hoffman, M. Cuntz, and P. Stoy, "Geostationary satellite observations can accurately estimate ecosystem carbon uptake and respiration at half hourly time steps at Eddy covariance sites," SSRN, 2023.

[9] A. Khan et al., "The diurnal dynamics of gross primary productivity using observations from the advanced baseline imager on the geostationary operational environmental satellite-R series at an Oak Savanna ecosystem," *J. Geophys. Res. Biogeosci.*, vol. 127, no. 3, 2022, Art. no. e2021JG006701.

[10] D. Losos, S. Hoffman, and P. C. Stoy, "GOES-R land surface products at Western Hemisphere eddy covariance tower locations," *Sci. Data*, vol. 11, no. 1, Mar. 2024, Art. no. 277, doi: 10.1038/s41597-024-03071-z.

[11] I. Laszlo, H. Liu, H.-Y. Kim, and R. T. Pinker, "Chapter 15 - shortwave radiation from ABI on the GOES-R Series," in *The GOES-R Series: A New Generation of Geostationary Environmental Satellites*, S. J. Goodman, T. J. Schmit, J. Daniels, and R. J. Redmon, Eds. Amsterdam, The Netherlands: Elsevier, 2020, pp. 179–191. doi: 10.1016/B978-0-12-814327-8.00015-9.

[12] J.-M. Yeom, S. Park, T. Chae, J.-Y. Kim, and C. S. Lee, "Spatial assessment of solar radiation by machine learning and deep neural network models using data provided by the COMS MI geostationary satellite: A case study in South Korea," *Sensors*, vol. 19, no. 9, 2019, Art. no. 2082.

[13] H. Jiang, N. Lu, J. Qin, W. Tang, and L. Yao, "A deep learning algorithm to estimate hourly global solar radiation from geostationary satellite data," *Renew. Sustain. Energy Rev.*, vol. 114, 2019, Art. no. 109327.

[14] S. Zhao et al., "Coupling meteorological stations data and satellite data for prediction of global solar radiation with machine learning models," *Renew. Energy*, vol. 198, pp. 1049–1064, 2022.

[15] D. Hao et al., "Estimating hourly land surface downward shortwave and photosynthetically active radiation from DSCOVR/EPIC observations," *Remote Sens. Environ.*, vol. 232, 2019, Art. no. 111320.
[16] R. Ma et al., "Estimation of surface shortwave radiation from Himawari-8 satellite data based on a combination of radiative transfer and deep neural network," *IEEE Trans. Geosci. Remote Sens.*, vol. 58, no. 8, pp. 5304–5316, Aug. 2020.
[17] R. Li, D. Wang, and S. Liang, "Comparison between deep learning architectures for the 1 km, 10/15-min estimation of downward shortwave radiation from AHI and ABI," *Remote Sens. Environ.*, vol. 295, 2023, Art. no. 113697.
[18] Z. Peng et al., "Estimation of shortwave solar radiation using the artificial neural network from Himawari-8 satellite imagery over China," *J. Quant. Spectrosc. Radiat. Transf.*, vol. 240, 2020, Art. no. 106672.
[19] J. Chen, W. Zhu, and Q. Yu, "Estimating half-hourly solar radiation over the continental United States using GOES-16 data with iterative random forest," *Renew. Energy*, vol. 178, pp. 916–929, 2021.
[20] S. Ranjbar, A. Zarei, M. Hasanlou, M. Akhoondzadeh, J. Amini, and M. Amani, "Machine learning inversion approach for soil parameters estimation over vegetated agricultural areas using a combination of water cloud model and calibrated integral equation model," *J. Appl. Remote Sens.*, vol. 15, no. 1, 2021, Art. no. 018503.
[21] H. Chu et al., "AmeriFlux BASE data pipeline to support network growth and data sharing," *Sci. Data*, vol. 10, no. 1, 2023, Art. no. 614.
[22] J. A. Augustine, J. J. DeLuisi, and C. N. Long, "SURFRAD–A national surface radiation budget network for atmospheric research," *Bull. Amer. Meteorol. Soc.*, vol. 81, no. 10, pp. 2341–2358, 2000.
[23] S. Metzger et al., "From NEON field sites to data portal: A community resource for surface–atmosphere research comes online," *Bull. Amer. Meteorol. Soc.*, vol. 100, no. 11, pp. 2305–2325, 2019.
[24] K. R. Knapp, R. Frouin, S. Kondragunta, and A. Prados, "Toward aerosol optical depth retrievals over land from GOES visible radiances: Determining surface reflectance," *Int. J. Remote Sens.*, vol. 26, no. 18, pp. 4097–4116, 2005.
[25] H. Zhang, S. Kondragunta, I. Laszlo, and M. Zhou, "Improving GOES advanced Baseline Imager (ABI) aerosol optical depth (AOD) retrievals using an empirical bias correction algorithm," *Atmos. Meas. Tech.*, vol. 13, no. 11, pp. 5955–5975, 2020.
[26] F. A. Diaz-Gonzalez, J. Vuelvas, C. A. Correa, V. E. Vallejo, and D. Patino, "Machine learning and remote sensing techniques applied to estimate soil indicators–review," *Ecol. Indic.*, vol. 135, 2022, Art. no. 108517.
[27] B. Thapa, S. Lovell, and J. Wilson, "Remote sensing and machine learning applications for aboveground biomass estimation in agroforestry systems: A review," *Agrofor. Syst.*, vol. 97, pp. 1097–1111, 2023.
[28] R. Varghese, A. K. Cherukuri, N. H. Doddrell, C. G. P. Doss, A. J. Simkin, and S. Ramamoorthy, "Machine learning in photosynthesis: Prospects on sustainable crop development," *Plant Sci.*, vol. 335, 2023, Art. no. 111795.
[29] J. H. Friedman, "Greedy function approximation: A gradient boosting machine," *Ann. Statist.*, pp. 1189–1232, 2001.
[30] E. K. Sahin, "Assessing the predictive capability of ensemble tree methods for landslide susceptibility mapping using XGBoost, gradient boosting machine, and random forest," *SN Appl. Sci.*, vol. 2, no. 7, 2020, Art. no. 1308.
[31] R. Saini and S. K. Ghosh, "Ensemble classifiers in remote sensing: A review," in *Proc. Int. Conf. Comput., Commun. Autom.*, 2017, pp. 1148–1152.
[32] Y. Zhang, J. Liu, and W. Shen, "A review of ensemble learning algorithms used in remote sensing applications," *Appl. Sci.*, vol. 12, no. 17, 2022, Art. no. 8654.
[33] H. Bahrami, S. Homayouni, M. Mahdianpari, and A. Safari, "Ensemble learning for crop monitoring from multitemporal optical and synthetic aperture radar earth observations," in *Proc. IEEE Int. Geosci. Remote Sens. Symp.*, 2021, pp. 5929–5932.
[34] C. Bentéjac, A. Csörgő, and G. Martínez-Muñoz, "A comparative analysis of gradient boosting algorithms," *Artif. Intell. Rev.*, vol. 54, pp. 1937–1967, 2021.
[35] S. Hochreiter and J. Schmidhuber, "Long short-term memory," *Neural Comput.*, vol. 9, no. 8, pp. 1735–1780, 1997.
[36] H. Ghanbari, M. Mahdianpari, S. Homayouni, and F. Mohammadimanesh, "A meta-analysis of convolutional neural networks for remote sensing applications," *IEEE J. Sel. Top. Appl. Earth Observ. Remote Sens.*, vol. 14, pp. 3602–3613, 2021.
[37] I. Sutskever, O. Vinyals, and Q. V. Le, "Sequence to sequence learning with neural networks," *Adv. Neural Inf. Process. Syst.*, vol. 27, 2014, pp. 3104–3112.
[38] M. Schuster and K. K. Paliwal, "Bidirectional recurrent neural networks," *IEEE Trans. Signal Process.*, vol. 45, no. 11, pp. 2673–2681, Nov. 1997.
[39] Q. Yuan et al., "Deep learning in environmental remote sensing: Achievements and challenges," *Remote Sens. Environ.*, vol. 241, 2020, Art. no. 111716.
[40] A. Baraldi, E. Binaghi, P. Blonda, P. A. Brivio, and A. Rampini, "Comparison of the multilayer perceptron with neuro-fuzzy techniques in the estimation of cover class mixture in remotely sensed data," *IEEE Trans. Geosci. Remote Sens.*, vol. 39, no. 5, pp. 994–1005, May 2001.
[41] M. W. Gardner and S. Dorling, "Artificial neural networks (the multilayer perceptron)—A review of applications in the atmospheric sciences," *Atmos. Environ.*, vol. 32, no. 14–15, pp. 2627–2636, 1998.
[42] A. Suliman and Y. Zhang, "A review on back-propagation neural networks in the application of remote sensing image classification," *J. Earth Sci. Eng.*, vol. 5, no. 1, pp. 52–65, 2015.
[43] H. Bahrami, S. Homayouni, A. Safari, S. Mirzaei, M. Mahdianpari, and O. Reisi-Gahrouei, "Deep learning-based estimation of crop biophysical parameters using multi-source and multi-temporal remote sensing observations," *Agronomy*, vol. 11, no. 7, 2021, Art. no. 1363.
[44] H. Shirmard et al., "A comparative study of convolutional neural networks and conventional machine learning models for lithological mapping using remote sensing data," *Remote Sens.*, vol. 14, no. 4, 2022, Art. no. 819.
[45] S. Ghimire, R. C. Deo, D. Casillas-Pérez, S. Salcedo-Sanz, E. Sharma, and M. Ali, "Deep learning CNN-LSTM-MLP hybrid fusion model for feature optimizations and daily solar radiation prediction," *Measurement*, vol. 202, 2022, Art. no. 111759.
[46] H. Dhake, Y. Kashyap, and P. Kosmopoulos, "Algorithms for hyperparameter tuning of LSTMS for time series forecasting," *Remote Sens.*, vol. 15, no. 8, 2023, Art. no. 2076.
[47] A. E. Maxwell, T. A. Warner, and F. Fang, "Implementation of machine-learning classification in remote sensing: An applied review," *Int. J. Remote Sens.*, vol. 39, no. 9, pp. 2784–2817, 2018.
[48] F. Pedregosa et al., "Scikit-learn: Machine learning in Python," *J. Mach. Learn. Res.*, vol. 12, pp. 2825–2830, 2011.
[49] S. M. Lundberg and S.-I. Lee, "A unified approach to interpreting model predictions," *Adv. Neural Inf. Process. Syst.*, vol. 30, pp. 4768–4777, 2017.
[50] S. M. Lundberg et al., "From local explanations to global understanding with explainable AI for trees," *Nat. Mach. Intell.*, vol. 2, no. 1, pp. 56–67, 2020.
[51] C. Molnar, G. Casalicchio, and B. Bischl, "iml: An R package for interpretable machine learning," *J. Open Source Softw.*, vol. 3, no. 26, 2018, Art. no. 786.
[52] H. Zhang et al., "Retrieving high-resolution surface photosynthetically active radiation from the MODIS and GOES-16 ABI data," *Remote Sens. Environ.*, vol. 260, 2021, Art. no. 112436.
[53] National Oceanic and Atmospheric Administration, "Aerosol optical depth at SURFRAD networks," 2022. [Online]. Available: https://gml.noaa.gov/grad/surfrad/aod/aod_check.php?site=tbl&date=2022-07-03&wavelength=500
[54] S. Liu, H. Fan, M. Ferianc, X. Niu, H. Shi, and W. Luk, "Toward full-stack acceleration of deep convolutional neural networks on FPGAs," *IEEE Trans. Neural Netw. Learn. Syst.*, vol. 33, no. 8, pp. 3974–3987, Aug. 2022.
[55] H. Liang, Z. Zhang, C. Hu, Y. Gong, and D. Cheng, "A survey on spatio-temporal big data analytics ecosystem: Resource management, processing platform, and applications," *IEEE Trans. Big Data*, vol. 10, pp. 174–193, Apr. 2024.
[56] L. J. Paxton, Y. Zhang, H. Kil, and R. K. Schaefer, "Exploring the upper atmosphere: Using optical remote sensing," in *Upper Atmosphere Dynamics and Energetics*. New York: NY, USA: Wiley, 2021, pp. 487–522.
[57] W. Tan, H. He, X. Chen, and W. Qi, "Analyzing the influence of atmosphere on optical remote sensing in 400 to 2500 nm wavelength spectrum," in *Proc. Opt. Spectrosc. Imag., Biomed. Opt.*, 2020, pp. 103–108.
[58] L. Rayleigh, "XXXIV. On the transmission of light through an atmosphere containing small particles in suspension, and on the origin of the blue of the sky," *Lond. Edinb. Dublin Philos. Mag. J. Sci.*, vol. 47, no. 287, pp. 375–384, 1899.
[59] L. Chen et al., "Estimation of surface shortwave radiation components under all sky conditions: Modeling and sensitivity analysis," *Remote Sens. Environ.*, vol. 123, pp. 457–469, 2012.
[60] M. Iqbal, *An Introduction to Solar Radiation*. Amsterdam, The Netherlands: Elsevier, 2012.
[61] N. Hou et al., "Estimation of surface downward shortwave radiation over China from Himawari-8 AHI data based on random forest," *Remote Sens.*, vol. 12, no. 1, 2020, Art. no. 181.

[62] L. Li et al., "A method for estimating hourly photosynthetically active radiation (PAR) in China by combining geostationary and polar-orbiting satellite data," *Remote Sens. Environ.*, vol. 165, pp. 14–26, 2015.
[63] Y. Kang, M. Kim, E. Kang, D. Cho, and J. Im, "Improved retrievals of aerosol optical depth and fine mode fraction from GOCI geostationary satellite data using machine learning over East Asia," *ISPRS J. Photogramm. Remote Sens.*, vol. 183, pp. 253–268, 2022.
[64] P. Minnis, G. Hong, S. Sun-Mack, W. L. Smith Jr, Y. Chen, and S. D. Miller, "Estimating nocturnal opaque ice cloud optical depth from MODIS multispectral infrared radiances using a neural network method," *J. Geophys. Res. Atmos.*, vol. 121, no. 9, pp. 4907–4932, 2016.
[65] Y. Yang et al., "Machine learning-based retrieval of day and night cloud macrophysical parameters over East Asia using Himawari-8 data," *Remote Sens. Environ.*, vol. 273, 2022, Art. no. 112971.
[66] G. Pastorello et al., "Observational data patterns for time series data quality assessment," in *Proc. IEEE 10th Int. Conf. e-Sci.*, 2014, pp. 271–278.
[67] G. Pastorello et al., "The FLUXNET2015 dataset and the ONEFlux processing pipeline for eddy covariance data," *Sci. Data*, vol. 7, no. 1, 2020, Art. no. 225.
[68] M. Aubinet, T. Vesala, and D. Papale, *Eddy Covariance: A Practical Guide to Measurement and Data Analysis*. Berlin, Germany: Springer Science & Business Media, 2012.
[69] Y. Zhang, S. Liang, T. He, D. Wang, Y. Yu, and H. Ma, "Estimation of land surface incident shortwave radiation from geostationary advanced Himawari imager and advanced baseline imager observations using an optimization method," *IEEE Trans. Geosci. Remote Sens.*, vol. 60, 2020, Art. no. 5600611.
[70] X. Li et al., "New-generation geostationary satellite reveals widespread midday depression in dryland photosynthesis during 2020 western US heatwave," *Sci. Adv.*, vol. 9, no. 31, 2023, Art. no. eadi0775.
[71] E. Jahan, R. E. Sharwood, and D. T. Tissue, "Effects of leaf age during drought and recovery on photosynthesis, mesophyll conductance and leaf anatomy in wheat leaves," *Front. Plant Sci.*, vol. 14, 2023, Art. no. 1091418.
[72] A. Massetti, C. Rüdiger, M. Yebra, and J. Hilton, "The Vegetation Structure Perpendicular Index (VSPI): A forest condition index for wildfire predictions," *Remote Sens. Environ.*, vol. 224, pp. 167–181, 2019.
[73] G. Xu and X. Zhong, "Real-time wildfire detection and tracking in Australia using geostationary satellite: Himawari-8," *Remote Sens. Lett.*, vol. 8, no. 11, pp. 1052–1061, 2017.
[74] A. Mohapatra and T. Trinh, "Early wildfire detection technologies in practice—A review," *Sustainability*, vol. 14, no. 19, 2022, Art. no. 12270.
[75] T. Hu et al., "Monitoring agricultural drought in Australia using MTSAT-2 land surface temperature retrievals," *Remote Sens. Environ.*, vol. 236, 2020, Art. no. 111419.
[76] J. A. Otkin et al., "Flash droughts: A review and assessment of the challenges imposed by rapid-onset droughts in the United States," *Bull. Amer. Meteorol. Soc.*, vol. 99, no. 5, pp. 911–919, 2018.
[77] S. Chen et al., "NIRvP as a remote sensing proxy for measuring gross primary production across different biomes and climate zones: Performance and limitations," *Int. J. Appl. Earth Observ. Geoinf.*, vol. 122, Aug. 2023, Art. no. 103437, doi: 10.1016/j.jag.2023.103437.
[78] S. Jeong et al., "Tracking diurnal to seasonal variations of gross primary productivity using a geostationary satellite, GK-2A advanced meteorological imager," *Remote Sens. Environ.*, vol. 284, Jan. 2023, Art. no. 113365, doi: 10.1016/j.rse.2022.113365.
[79] A. M. Khan et al., "The diurnal dynamics of gross primary productivity using observations from the advanced baseline imager on the geostationary operational environmental satellite-R series at an Oak Savanna ecosystem," *J. Geophys. Res. Biogeosci.*, vol. 127, no. 3, 2022, Art. no. e2021JG006701.
[80] H. Letu et al., "A new benchmark for surface radiation products over the East Asia–Pacific region retrieved from the Himawari-8/AHI next-generation geostationary satellite," *Bull. Amer. Meteorol. Soc.*, vol. 103, no. 3, pp. E873–E888, 2022.

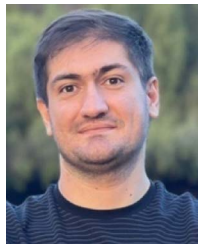

Sadegh Ranjbar (Graduate Student Member, IEEE) received the B.Eng. degree in surveying and geomatics engineering from the Faculty of Civil Engineering, Shaheed Rajaei Teacher Training University, Tehran, Iran, in 2017, and the M.Eng. degree in remote sensing from the College of Engineering, University of Tehran, Tehran, Iran, in 2021. He is currently working toward the Ph.D. degree with the University of Wisconsin–Madison, Madison, WI, USA.

He is particularly passionate about using artificial intelligence and machine learning methods to analyze different remote sensing datasets, especially for urban and agro-environmental purposes. His research interests include near real-time carbon cycle mapping using geostationary satellites observations.

Danielle Losos received the B.S. degree in environmental science degree from the Yale College, New Haven, CT, USA, in 2022.

During an undergraduate gap-year, she worked with NOAA for the GOES-R Product Readiness and Operations team in Greenbelt, MD, USA. Since graduating, she was with the Space Science and Engineering Center (SSEC) and the Department of Biological System Engineering, University of Wisconsin–Madison, Madison, WI, USA. Her current research interests include underutilized satellite products to tackle environmental challenges, including real-time carbon cycling and wildfire mapping.

Sophie Hoffman received the B.S. degree in atmospheric sciences and applied mathematics from the University of Wisconsin–Madison, Madison, WI, USA, in 2020.

During her time as an undergraduate, she worked with the UW-Madison Space Science and Engineering Center with remote sensing data from the Venus Climate Orbiter (Akatsuki) to study the causes and effects of the absorption of light and radiation within the Venusian atmosphere. Since 2022, she has been working with the Department of UW-Madison Biological Systems Engineering, Madison, WI, USA, on a project to develop a near real-time mapping of the carbon cycle using geostationary satellite and eddy covariance tower observations.

Paul C. Stoy received the B.A. degree in zoology and botany from the University of Wisconsin–Madison, Madison, MI, USA, in 2001, the Ph.D. degree in ecology from Duke University, Durham, NC, USA, in 2006, and the Ph.D. training in ecology with the University of Edinburgh, Edinburgh, U.K.

He was Assistant then Associate Professor with Montana State University before beginning a faculty position at the University of Wisconsin–Madison, where he is a Professor with the Department of Biological Systems Engineering.